Hino *et al.*
Progress in Earth and Planetary Science (2022) 9:73
https://doi.org/10.1186/s40645-022-00526-y

Progress in Earth and Planetary Science

RESEARCH ARTICLE

Open Access

Assessment of S-net seafloor pressure data quality in view of seafloor geodesy

Ryota Hino[1*], Tatsuya Kubota[2], Naotaka Y. Chikasada[2], Yusaku Ohta[1] and Hideto Otsuka[1]

Abstract

Long-term continuous observation of seafloor pressure is effective for detecting seafloor vertical deformations that are associated with transient tectonic phenomena such as slow slip events. Since the aseismic slip event prior to the 2011 Tohoku earthquake, several discoveries have been made on spontaneous slow slip events and various other types of slow earthquake along the Japan and Kuril Trenches. Seafloor observation network for earthquakes and tsunamis along the Japan Trench (S-net) is expected to provide invaluable information on slow slip activities via geodetic signals that are detected by pressure observation. This study inspects the quality of the S-net pressure data in view of seafloor geodesy by comparison with records obtained by more than 100 autonomous ocean bottom pressure recorders (OBPRs) deployed along the Japan Trench. OBPRs have long been standard tools in seafloor geodesy, and the data collected are considered a benchmark in terms of quality. Most of the S-net stations showed noise levels that are considerably higher than those of the OBPRs over periods of more than 2 d. We speculate that a strong correlation between pressure and temperature accounts for much of the long-term noise. In this study, the temperature-dependent fluctuation component was estimated by prediction filtering and removed from the original data, leading to a significant reduction in the noise level at 51 stations, which reached levels almost equivalent to those of OBPRs. Although no significant pressure changes have been identified as associated with the 2018 Boso SSE or repeated tremor bursts in the northern Japan Trench thus far, our findings indicate that these stations are sufficiently sensitive to detect slow slip events occurring nearby.

Keywords: S-net, Seafloor pressure observation, OBPR, Slow slip events, Pressure–temperature correlation

1 Introduction

The 2011 Tohoku earthquake triggered an increase in research in the number of studies on the slow slip activity that occurs along the Japan and Kuril Trenches. The slow slip that preceded the main shock was indicated by analysis of foreshock and tectonic tremor activities (Kato et al., 2012; Ito et al., 2015; Katakami et al., 2018) and seafloor pressure observations (Ohta et al., 2012; Ito et al., 2013); the relationship between slow slips and the occurrence of large earthquakes has thus attracted attention (Obara and Kato, 2016). Accelerating aseismic slips in this region have also been reported as afterslips following major earthquakes (Kawasaki et al., 1995; Heki et al., 1997; Iinuma et al., 2016; Itoh et al., 2019). Ohta et al. (2019) reported on the tectonic tremor activity promoted by the afterslip of the 2011 Tohoku earthquake in the shallow plate boundary in the southern Japan Trench. However, evidently, spontaneously accelerating slips occur not only immediately after major earthquakes, but also continuously and periodically (Uchida et al., 2016). Recently, frequent very low frequency earthquakes, a type of slow earthquake, have been reported by onshore broadband seismic observations in the region (Matsuzawa et al., 2015; Baba et al. 2020).

The 2011 Tohoku earthquake led to the development of an offshore observation network, Seafloor observation network for earthquakes and tsunamis along the Japan

*Correspondence: hino@tohoku.ac.jp

[1] Graduate School of Science, Tohoku University, 6-6 Aramaki-Aza-Aoba, Aoba-Ku, Sendai, Miyagi 980-8578, Japan
Full list of author information is available at the end of the article

Trench (S-net), which was established to observe submarine earthquakes and tsunamis (Aoi et al., 2020). Using S-net short-period seismograms, Nishikawa et al. (2019) and Tanaka et al. (2019) discovered that tectonic tremor activity is widely distributed over the shallow part of the subduction zone across the Japan Trench and the southwestern edge of the Kuril Trench. This finding strongly suggests the occurrence of shallow slow slip events (SSEs) in the subduction zone. However, most SSEs occur away from the terrestrial geodetic networks that cannot detect the associated crustal deformation. Thus, only Honsho et al. (2019) indicated an association between the horizontal displacement resulting from an SSE and an increase in the number of small repeating earthquakes in 2015, which was detected by a series of campaign surveys using GNSS-Acoustic seafloor measurement.

Compared to that of the SSEs that occur on the downdip side of the seismogenic zone, knowledge of shallow SSEs is based on only a few observations. However, shallow SSE activity is key to understanding the frictional behavior that occurs at shallow plate boundaries, which has been the focus of attention since the Tohoku earthquake, when a seismic slip reached the trench axis (Fujiwara et al. 2011; Iinuma et al., 2012; Kodaira et al, 2020). Seafloor pressure observation is expected to be an effective tool for shallow SSE observation because it enables long-term continuous observation of the vertical movement of the Earth's surface just above the shallow boundary of the plate. Crustal deformation due to an SSE off Hikurangi in 2014 was observed by both the terrestrial geodetic network and a network of autonomous ocean bottom pressure recorders (OBPRs), indicating that the slip extended close to the trench axis (Wallace et al., 2016). Seafloor pressure observations are thus being conducted in several locations globally (Davis et al., 2015; Fredrickson et al., 2019).

The main purpose of the S-net is to detect offshore tsunamis, and it has thus far provided important information concerning various tsunami events (Kubota et al. 2021a, 2021b, 2022). Kubota et al. (2020) detected tsunamis with a wave height of less than 1 cm that were generated by a local M 6.0 earthquake just below the network, indicating the high resolution of S-net pressure observation in a short-period band of less than 1 h. If the sensitivity to water pressure changes, such as those associated with SSEs, remains constant over a longer period and is as high as it is in the tsunami frequency range, we can expect SSEs to be detected from pressure data obtained continuously over longer periods by the broad seafloor pressure monitoring network. Seafloor pressure gauges sense vertical changes in the elevation of the seafloor after removing fluctuations due to the motion of the overlying oceans and atmosphere (Bürgmann and Chadwell, 2014; Wilcock et al., 2021). OBPRs, which are capable of continuous observation for 1 to 2 years, have thus far been used for SSE detection (e.g., Ito et al., 2013; Wallace et al. 2016). However, OBPR observations are limited with respect to both period and spatial coverage. Observation data from a wide-area multi-point observation network are expected to provide a more comprehensive picture of SSE activity. Suzuki et al. (2016) reported on a possible shallow SSE based on the pressure data that were obtained from the Dense Ocean floor Network system for Earthquakes and Tsunamis (DONET), which is deployed along the Nankai Trough. In this paper, the quality of S-net pressure records obtained at lower frequencies than those focused upon in tsunami observations was evaluated and the possible detection of crustal deformation resulting from shallow SSEs was discussed.

This study focused on the power spectrum of the S-net pressure data to investigate the characteristics over a wide frequency range and compare them with OBPR data previously obtained for the Japan Trench. We found that the noise level at many S-net stations was more than 10 times higher than that associated with OBPR in the frequency bands of geodetic interest, rendering it difficult to detect small crustal deformations at the cm level, while the noise level was at least as high as that associated with data collected by OBPRs at the remaining 51 stations. Deformation that was associated with SSE events with magnitudes > Mw 6 occurring in the vicinity of such quiet stations is therefore likely to be detected.

2 Data

2.1 S-net seafloor pressure observation

Although the details of the S-net system have previously been described by Aoi et al (2020), we reiterate the part that is related to pressure observation in this section. S-net consists of 150 seafloor seismic and water pressure stations (Fig. 1). The network is divided into six submarine fiber networks; subsystems S-1 to S-5 along the landward slope of the trench, and S-6, which is deployed on the incoming plate outside the trenches. The observation equipment is packed into anti-pressure cylindrical housing that is separated into wet and dry sections. The pressure sensors are placed in the wet section, filled with fluid and is isolated from seawater by bellows and diaphragm, constructed using flexible materials that allow equivalency of internal and external pressure. The dry section contains devices such as seismic sensors, electronic signal amplification and processing units, communication equipment, and power supply. The instruments at each station belonging to one subsystem are connected serially via submarine cables, much like the repeaters used for commercial communication. Observation systems that use this type of geometry are known as inline

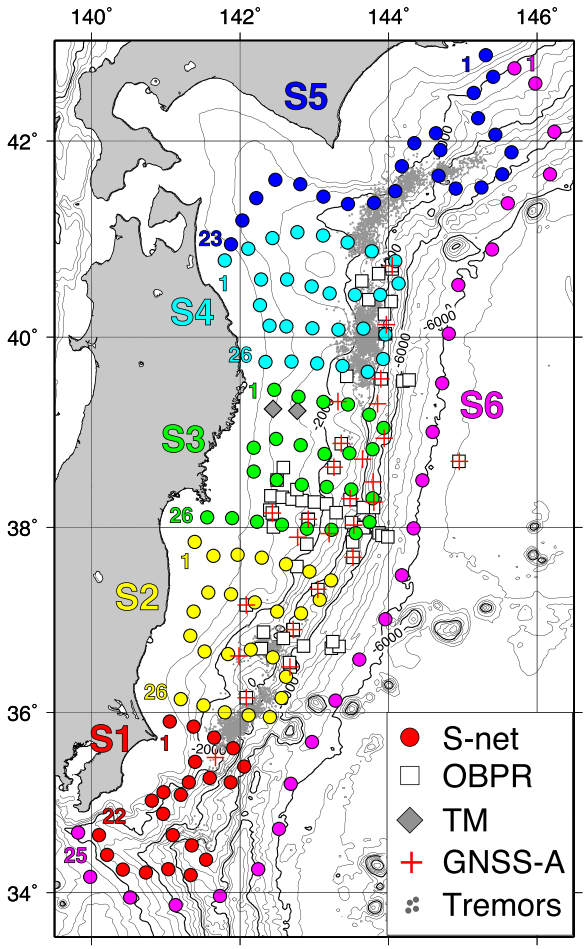

Fig. 1 Map showing distribution of the observation points (stations). Circles indicate S-net stations and are colored according to subsystems. Squares show locations of OBPRs deployed from 2008 to 2019. Not all stations were operating simultaneously. Diamonds denote stations in the TM system. Crosses are seafloor benchmarks in the GNSS-Acoustic geodetic survey. Epicenters of tectonic tremors (Nishikawa et al., 2019) are plotted as gray dots. Water depth contours are in 500-m intervals

systems, and a similar structure is used in many other cable-based submarine earthquake and tsunami observation systems in Japan (Kanazawa and Hasegawa, 1997; Hirata et al., 2002).

As the location where the instruments are installed is an active trawl fishing area, instruments were placed beneath the seafloor in water at depths of up to 1500 m, which is the operational range for trawling. The instruments were buried using a plow-type burial machine, which is also used for laying commercial submarine cables, and covered by soft sediments just below the seafloor to a thickness of several tens of centimeters. Meanwhile, the instruments at the stations in water depths of more than 1500 m were not buried and just placed on the seafloor.

2.2 Characteristics of S-net data

The sensor, Paroscientific 8B7000-2–005 or 8B8000-2–005, provides continuous recording of pressure and temperature at a sampling frequency of 10 Hz. To investigate the nature of the seafloor pressure data for the purpose of detecting crustal deformation, continuous data comprising 1-h samples for the period from the beginning of observation in May 2016 to June 2022 were generated and analyzed. Power spectra for all 150 stations were obtained, allowing us to attain an overall picture of the characteristics obtained by S-net. The spectra were obtained using a moving 4096-h time window that was shifted 24 h, and the median value was taken as the representative spectrum for each individual observation station. An example of an obtained power spectra is shown in Additional file 1: Fig. S1a. Significant diversity was observed in the power spectra for the different stations (Additional file 1: Fig. S1b); thus, a probability density distribution of the power spectrum was created to understand the characteristics of this diversity (Additional file 1: Figs. S1c and Fig. 2a). The results show that the S-net stations can be classified according to the characteristics of the pressure data in the frequency domain.

The power spectra show broad distribution at the lowest frequency. To observe the variation in power for the lower frequency components, root-mean-square (RMS) amplitudes of the pressure records were obtained by applying a low-pass filter with a cutoff frequency of 1.39E-3 cph (cycles per hour) or a period of 30 d, 3.86E-7 Hz (1 cph = 2.78E-4 Hz). The inherent sensor drift in the pressure sensors is a well-known cause of long-period variation (Watts and Kontoyiannis, 1990; Polster et al., 2009). Therefore, the RMS was calculated after the drift, expressed as exponential plus linear function of time, and subtracted from the filtered waveform.

Figure 3a shows the difference in the RMS for pressure data obtained at all S-net stations. Considering that 1 hPa of water pressure change is roughly equivalent to 1 cm of vertical seafloor motion, it would be difficult to detect crustal deformation at stations where the RMS is > 10 hPa or 10 cm. Figure 4a and 4b shows examples of pressure records with large RMS. The records from station 'a', indicated in Fig. 3a (Fig. 4a) showed annual variations with large amplitudes that are highly correlated with changes in the temperature, whereas irregular fluctuations were observed in the records from station 'b' (Fig. 4b). These fluctuations were not correlated with temperature variation and were suspected to be due to the mechanical instability of the instruments that are associated with pressure sensing. The S-net pressure

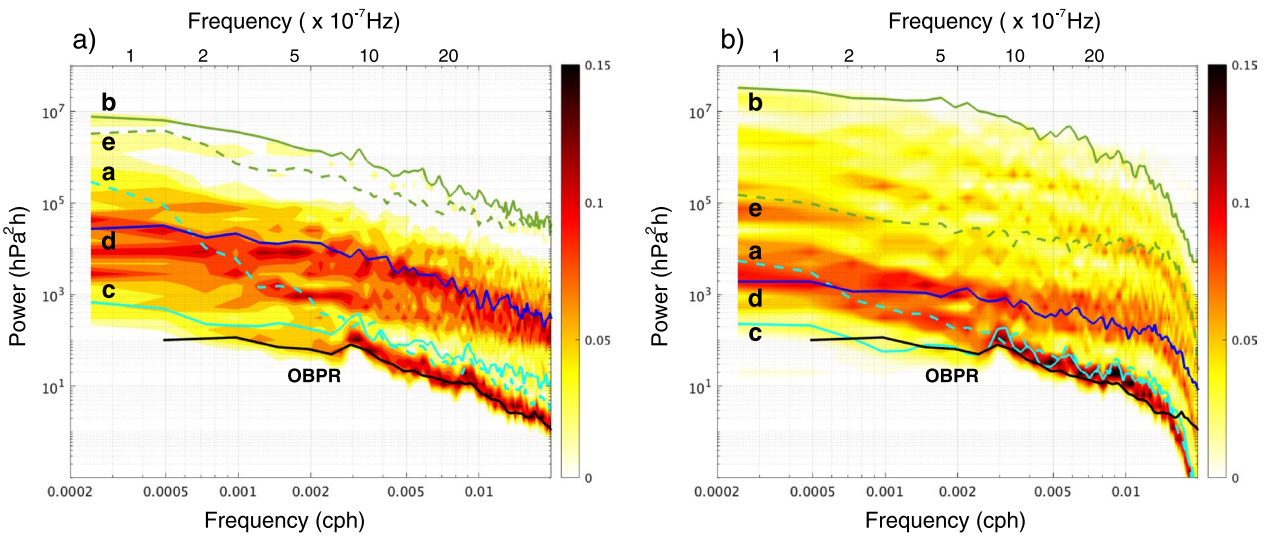

Fig. 2 Probability density of S-net pressure power spectra. **a** Raw pressure data. **b** Temperature-corrected pressure data. Curves 'a' to 'e' are the pressure spectra at the corresponding stations shown in Fig. 3a

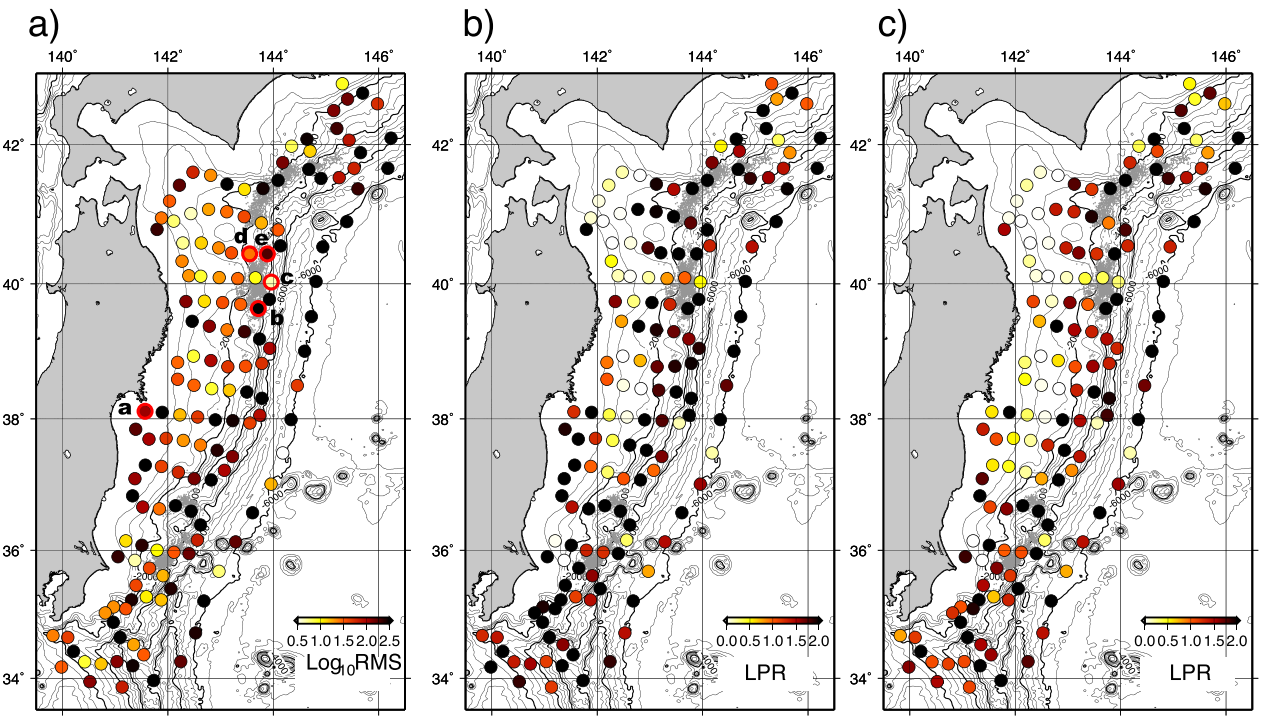

Fig. 3 Noise level of S-net stations defined by various quantities. **a** Root-mean-square (RMS) amplitude of long-period (longer than 30 d) component. RMS was calculated after the drift, expressed as exponential plus linear function of time, was subtracted from the filtered waveform. Pressure power spectra and pressure/temperature records obtained at stations indicated as 'a' to 'e' are shown in Fig. 2 and Fig. 4, respectively. **b** Logged power ratio (LPR) before temperature correction. **c** LPR following temperature correction. LPRs are calculated from 24 to 720 h in period

data also suffered from other factors that may reduce long-term stability, such as offsets due to strong ground motions that are irrelevant to the static displacement resulting from fault motions (Kubota et al., 2020), suggesting that it is difficult to detect long-term fluctuations exceeding one month from the S-net pressure data.

Focusing on frequency bands that are higher than 0.001 cph or for periods of < 1000 h, there are two prominent peaks in the probability density of the spectral shape (Fig. 3a). One peak lies around the lowest power level in the entire spectrum, and we classified stations with this peak as Group 1. The other peak is located at a power level of approximately a couple of hundred times higher than that observed in the results of Group 1. Stations with this peak comprised the majority of the S-net stations and were classified as Group 2. A few other stations demonstrated much higher power than the average power observed in Group 2.

An example of the records from a station in Group 1 ('c') is shown in Fig. 4c. The RMS for the long period was 4.5 hPa, which is one of the lowest among all stations. Although the record at station 'a' (Fig. 4a) has a large, long-period RMS (110.2 hPa), its power spectrum was close to that of Group 1 at high frequencies. The power spectrum was quiet in the short-period band, but rapidly and abruptly increased in the long-period side.

Examples of waveforms obtained at a Group 2 station ('d') and a station with much higher power ('e') are shown in Fig. 4d and 4e, respectively. The pressure fluctuations obtained at these stations may have a clear correlation with temperature changes.

Long-period instability can be expected to be removed as linear trends for periods of less than one month or thereabouts (~720 h). If the level of fluctuation within this period is small, it may be possible to detect short-term transient signals such as those caused by short-term slow slip events, even at stations with large, long-period fluctuations such as station 'a'.

The power spectra of the S-net observations were compared with those obtained by OBPRs, which have been proven to be sufficiently quiet to detect small tectonic signals (Ito et al., 2013; Hino et al., 2014; Wallace et al, 2016). The OBPR records are expected to more accurately elucidate the actual pressure variation on the seafloor because OBPR sensors are directly exposed to seawater. The probability density distribution of the OBPR power spectrum using records obtained from 122 OBPRs, which have been deployed since 2008 by Tohoku University, is shown in Additional file 2: Fig. S2. All deployed OBPRs were equipped with pressure sensors in the Paroscientific 8000 series, with specifications identical to those used in S-net. The time window for spectral estimation was set to 2048 h because of the short observation period over which the OBPRs function. The shape of the power spectrum was stable with little variation although the OBPRs were deployed at various times and locations. Therefore, the median value of the OBPR power spectra can be regarded as the standard for seafloor pressure changes in this area. Superimposing the median spectrum onto the probability density of the S-net power spectra (Fig. 2a) indicates that almost all of the S-net data are much noisier than the average OBPR data in all frequency bands, and this difference may be due to noise that is inherent in the S-net data.

As an indication of the quality of the S-net data, the logged power ratio (LPR) was calculated as follows:

$$\mathrm{LPR}_k = \frac{1}{N}\sum_{i=1}^{N}\left(\log_{10} P_k^{\text{S - net}}(f_i) - \log_{10} P^{\mathrm{OBPR}}(f_i)\right) \tag{1}$$

where $P_k^{\text{S - net}}(f_i)$ represents the pressure power at the kth S-net station, ith frequency band; $P^{\mathrm{OBPR}}(f_i)$ represents the median of the OBPR spectra at the ith frequency band; $\left(\log_{10} P_k^{\text{S - net}}(f_i) - \log_{10} P^{\mathrm{OBPR}}(f_i)\right)$ represents the deviation of the S-net logged power from the OBPR logged power at the ith frequency band; and LPR_k represents the mean of the deviations in the frequency range ($i = 1$, N), namely from 1.4E-3 to 2.1E-2 cph or from 24 to 720 h.

The LPRs of the data from the Group 1 stations are distributed over a range of < 1. Compared to the OBPR data, the pressure data obtained at these stations differ by a factor of 10 in terms of power, or by up to a factor of 3 in amplitude, and may thus be useful for detecting of transient tectonic signals. Figure 3b shows the LPRs for all the S-net stations, and it is apparent that several stations with small LPRs are located near zones with active tectonic tremor.

3 Results

3.1 Reduction in temperature dependence

As apparent in the pressure and temperature records in Fig. 4, high correlations were observed between the pressure and temperature variations. Histograms of the cross-correlations and the lag times that produce the maximum correlations are shown in Fig. 5. Lag (h) is positive when the pressure record appears to result from a temperature lag. The cross-correlation coefficients were nearly 1 at most stations. It should be noted that negative lag times dominated the results. The clear peak at ~ −8 h indicates that changes in temperature lead to pressure changes after ~ 8 h. Such significant temperature correlations were not observed in the OBPR data and are considered to be inherent in S-net records.

It is unlikely that inaccurate temperature compensation for the pressure sensor output accounts for the high correlation. If it were, the time lag would be shorter. The temperature-dependent pressure variation would be in the form of mechanical noise resulting from the structure of the observation device. Since the correlation seems to be more prominent at noisier stations (Fig. 4), we can assume that the dependence

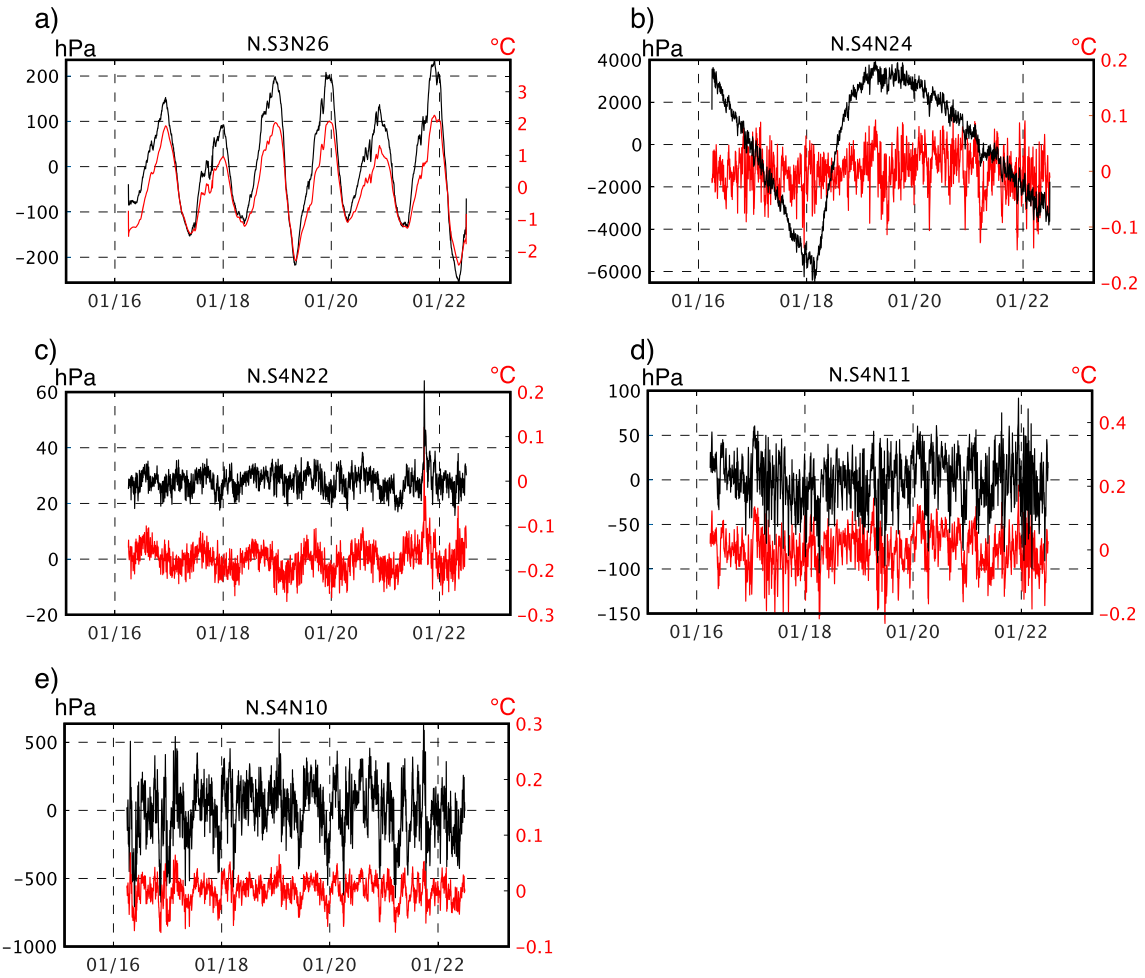

Fig. 4 Examples of pressure (black) and temperature (red) records. Typical examples with different pressure change characteristics are shown. **a** Example of large periodic fluctuations. **b** Example of slow and large irregular variations. **c** Example of small-amplitude fluctuations. **d** Moderate-amplitude high-frequency fluctuations. **e** Large-amplitude high-frequency fluctuations. Subpanels **a–e**) are records at stations 'a' to 'e' in Fig. 3a

of pressure fluctuation on temperature changes is the major source of noise in the S-net pressure data. If it can be eliminated, the signal-to-noise ratio of the pressure data may be improved.

To reduce the effect of temperature variation, prediction filtering was applied to the pressure and temperature records. A filter that predicts the apparent temperature-dependent pressure variation from the temperature record and subtracts the output of the filter from the pressure record was expected to remove any noise resulting from temperature disturbances. We assume that the observed pressure fluctuation consists of the sum of the apparent pressure fluctuation and the true pressure fluctuation:

$$p(t) = \hat{p}(t) + p'(t, T) \tag{2}$$

where $p(t)$ is the observed value,$p'(t, T)$ is the apparent pressure fluctuation due to the temperature disturbance, and $\hat{p}(t)$ is the true pressure fluctuation.

We further assume that the apparent pressure variation can be obtained from the temperature time series $T(t)$ by applying filter F:

$$p'(t, T) = F(t) * T(t). \tag{3}$$

Here, the asterisk denotes convolution. OBPR observations indicate that the actual seafloor pressure does not correlate with temperature. Therefore, the equation below can be used to estimate the filter coefficients by the least-square method.

$$F(t) * T(t - \tau) = p(t). \tag{4}$$

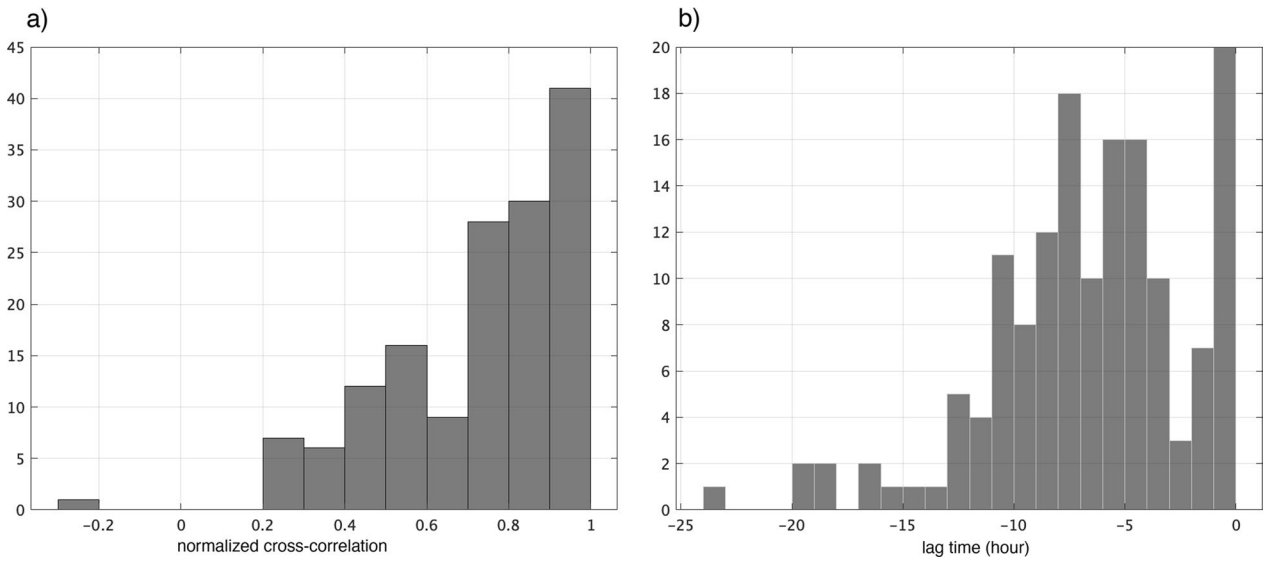

Fig. 5 Histograms of **a** normalized cross-correlations between pressure and temperature, and **b** lag times of pressure changes following temperature changes

Note that time shift τ (< 0) needs to be applied to ensure causality in the S-net data because $p(t)$ leads to $T(t)$ lag. Once a filter that can predict the apparent pressure variation from temperature is obtained, the true pressure variation can be determined using the predicted error and is expressed using the following equation:

$$\hat{p}(t) = p(t) - F(t) * T(t - \tau). \tag{5}$$

Since the filter estimation is equivalent to the division in the frequency domain,

$$F(f) \propto \frac{P(f)}{T(f)}, \tag{6}$$

the filter coefficients can diverge if the temperature spectrum $T(f)$ is much smaller than pressure spectrum $P(f)$ in a certain frequency range. In such cases, a component proportional to the time-shifted temperature $T(t - \tau)$ is subtracted from $p(t)$.

To evaluate the effect of the temperature correction using least-square filtering, the corrected S-net pressure records were compared with the pressure record obtained by an OBPR located ~ 4 km from station 'c' (Fig. 6). The LPR which was 0.50 before the temperature change decreased to 0.28 as a result of the temperature correction. Although there is a high similarity between the corrected waveform and the OBPR waveform, the long-period component is not in good agreement. However, we found that the similarity increased after a band-pass filter that covered the 48–720-h period component was applied to both this station and the S-net data following temperature correction.

Figure 2b shows the probability density of the power spectra obtained by applying the temperature correction to the results from all stations. The power was significantly reduced for stations in Group 2, to which most S-net stations belong. The Group 1 stations also showed improvement, as demonstrated in the above example (station 'c'), and the noise level was significantly reduced by removing the components correlated with temperature for many of the stations. However, the gap between Groups 1 and 2 remains, although it has been reduced. In addition, at stations where long-period irregular variations that do not correlate with temperature predominate [e.g., station 'b' (Fig. 4b)], the noise level has increased due to the temperature correction, leading to a relative increase in the frequency of higher power compared to the levels prior to correction.

The spatial distribution of LPRs in the temperature-corrected data is shown in Fig. 3c. Compared to Fig. 3b, the number of stations with LPR < 1, which is the noise level expected for OBPRs, increased from 40 before the correction to 51 after the correction. However, the LPRs are still > 1 at many stations even after correction, and stations that can detect small tectonic transients are limited and sparsely distributed along the Japan and Kuril Trenches.

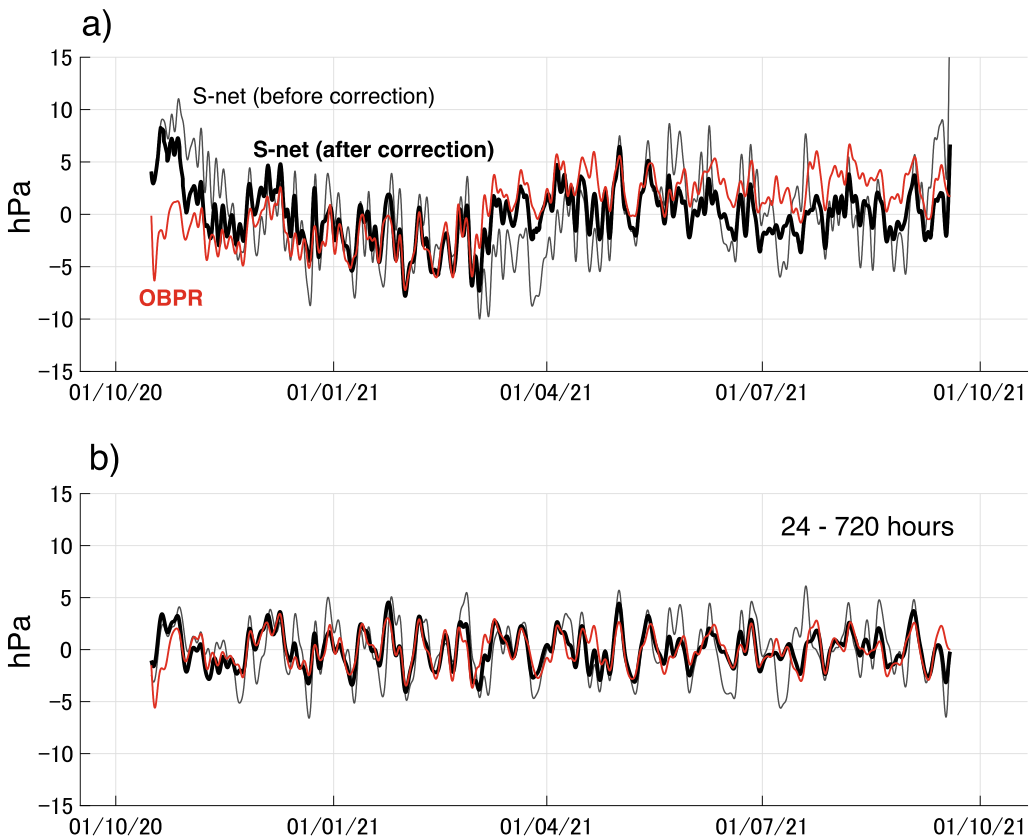

Fig. 6 Waveforms of S-net pressure data before (gray) and after temperature correction (black). Red traces show pressure data obtained by the OBPR located ~ 4 km from a S-net station. **a** Before application of band-pass filter. **b** After a pass-band filter was applied for 24 to 720 h

3.2 Reduction in common-mode noise

Examples of the temperature-corrected records of stations with a LPR < 1 are shown in Fig. 7a. As data gaps can introduce noise, time periods were selected in which continuous records from all stations with a LPR < 1 were recorded without any data gaps. Although a significant variation was observed in the noise level among all stations, the temperature-corrected time series shows a coherent component attributed to pressure disturbances of a non-tidal oceanographic origin. Several methods have been proposed to reduce such disturbances in order to increase the detectability of tectonic signals in the seafloor pressure data. Examples include a deterministic approach in which the seafloor pressure fluctuations calculated by ocean circulation models were subtracted from the results of observation (Inazu et al., 2012; Muramoto et al., 2019; Dobashi and Inazu, 2021), and estimation using obtained auxiliary oceanographic observations (Watts et al., 2021). Another is to find a proxy of the oceanographical fluctuation using a combination of pressure observations obtained in different locations. Here, we try to apply the latter approach.

One method that is often used for common-mode noise reduction is to use the pressure difference from a reference station (Ito et al., 2013) located far from the source location of the tectonic event representing the oceanographic signals. Wallace et al. (2016) set a reference station on the incoming plate side of the trench, where no vertical variations were expected, to detect an SSE signal in the OBPR data distributed on the landward slope. Fredrickson et al. (2019) and Inoue et al. (2021) showed that the non-tidal oceanographic fluctuations tend to be coherent among the sites located at stations with similar water depth and pointed out the advantage of using common-depth station pairs to obtain pressure differences with reduced noise.

Records that were obtained from stations on the incoming plate and landward sides with similar water depths were extracted from the high-quality S-net records obtained at 51 quiet stations (LPR < 1 after the temperature correction) in Fig. 7a and are displayed in Fig. 7b. The waveforms at stations 3–20 and 4–22 on the landward side of the trench were notably similar; however, few correlations were observed between the other

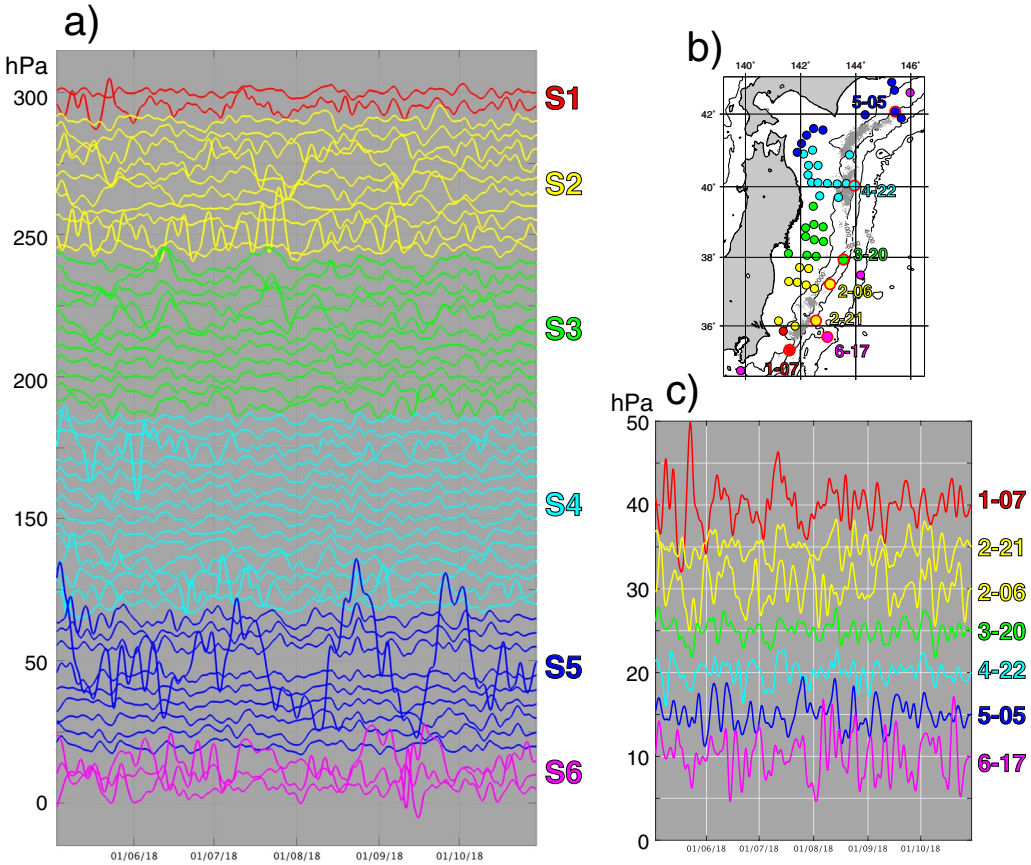

Fig. 7 **a** Pressure records after the temperature correction at stations with LPR < 1. **b** Station distribution. **c** Traces of selected stations close to the depth contour of 4000 m and a station on the incoming plate. Locations of selected stations are highlighted in **b**

stations. S-net does not provide a high degree of freedom in the combination of stations used for common-mode noise reduction via pressure difference. The difference between the records from stations 3–20 and 4–22, with relatively high similarity, was therefore investigated to test the theory, and we found that the RMS of the pressure data at station 3–20 was 1.14 and that at station 4–22 was 1.25, showing a reduction of 1.02 hPa.

Hino et al. (2014) showed that the common-mode noise can be reduced by subtracting the first principal component obtained by principal component analysis (PCA) without the use of pressure differences from a reference station. Similarly, we attempted to remove the common-mode noise in the S-net data in the same way. In applying PCA to the S-net data, it should be noted that the noise level varies greatly across stations. Here, we performed PCA weighted by the inverse of the variances of input temperature-corrected pressure data. Additional file 3: Figure S3 shows the results of PCA using all the records shown in Fig. 7a. The common-mode variations were reduced by subtracting the estimated first principal component. To evaluate the effect of PCA-based noise reduction, we determined the reduction rate of RMSs at all the stations and calculated their median, which was 81%. At stations 3–20 and 4–22, where we attempted to reduce the common-mode noise by taking pressure differences, the RMS decreased from 1.14 to 0.82 (72% reduction) and from 1.25 to 1.07 (86%), respectively.

From Fig. 7a, the non-tidal oceanographic component was not necessarily coherent over a wide area, and the correlation of waveforms decreased with increasing distance between stations. We, therefore, expected the noise reduction using PCA to be more effective if the range of stations used was limited to a relatively narrow area. Below, we applied the PCA-based common-mode noise reduction to the pressure records obtained at 13 quiet stations belonging to the S-4 system in the northern part of the Japan Trench. We chose these stations because their number and density of quiet stations were the largest in the region (Fig. 7b).

Figure 8a shows the temperature-corrected pressure records and the first principal components obtained

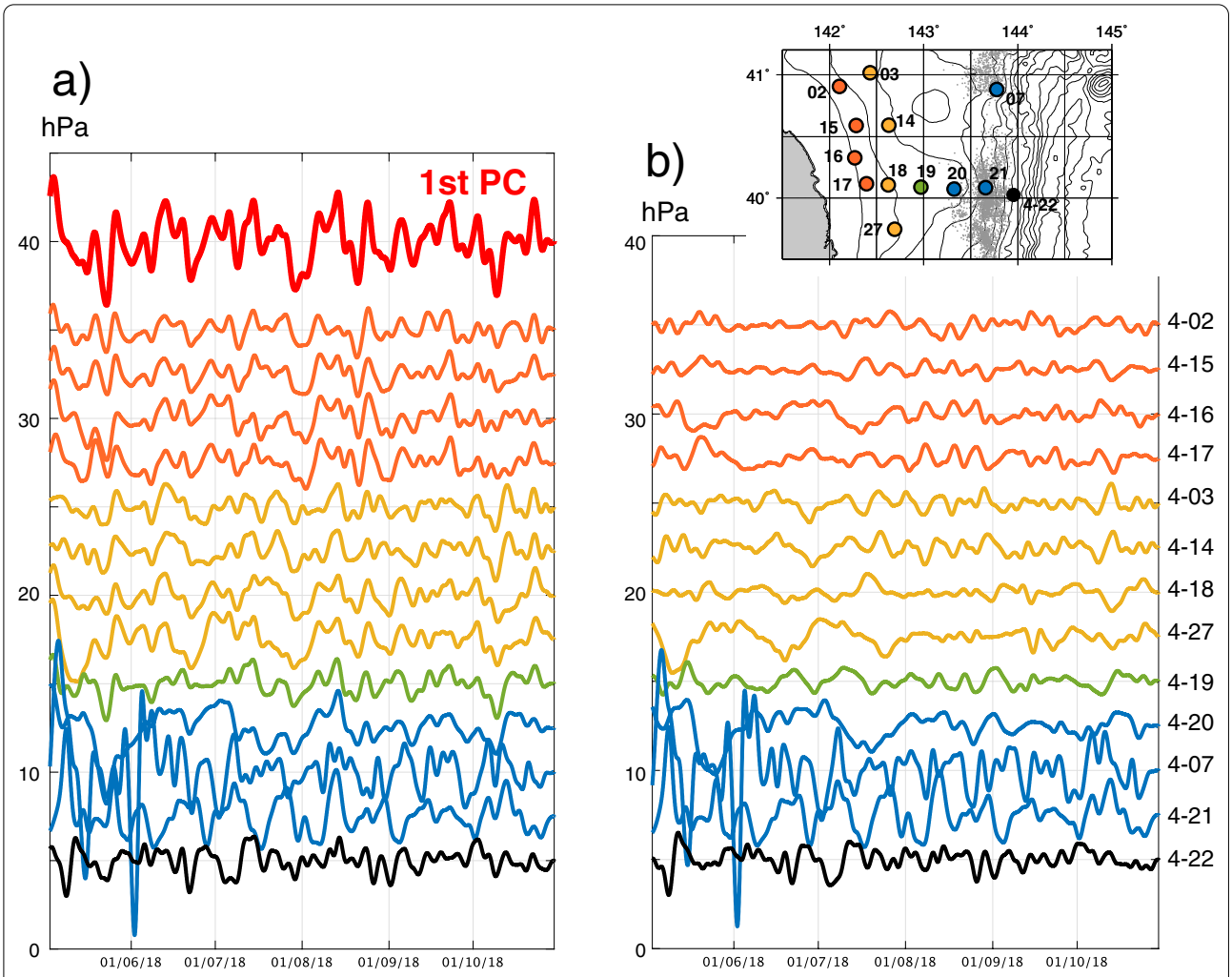

Fig. 8 **a** Pressure records after correction with LPR < 1 at stations belonging to S-4. Traces are colored according to the depth at which stations are located. Thick, red trace at the top is the first principal component (1st PC) obtained by PCA. **b** Pressure records after subtracting the 1st PC

from the temperature-corrected pressure records at the S-4 quiet stations selected from Fig. 7a. The color of the traces changes according to the depth of the stations, and it is apparent that the correlation was high between stations at similar depths, whereas the similarity of the waveforms decreased when stations at different depths were compared. Figure 8b shows the pressure records after the contribution of the first principal component was subtracted. The median of the RMS reduction rate was 66%, indicating a better performance when using stations within a narrow subarea than that when using broad network data. However, the noise reduction rate at station 4–22 was 89% (from 1.25 to 1.11), slightly worse than that after the noise reduction using broad network data.

One possible reason for the poor performance at the station can be the water depth dependence of waveform similarity. Station 4–22 was the deepest one among the quiet S-4 stations, the only station deployed at ~ 4,000 m depth, whereas six more stations located at depths similar to 4–22 were included in the PCA using all the quiet stations. The water depth-dependent components would be extracted as principal components of second or higher orders. However, subtracting the second principal component did not substantially reduce the RMS values. The reduction rates between the records after removing the first component and those after removing the first and second components were 96% and 86%, when applied to all the quiet stations and to the S-4 stations, respectively. The high level of instrumental noise likely remained in the record even after the temperature correction, and the noise hinders the extraction of depth-dependent components.

4 Discussion

4.1 Processed OBP records describing short-term SSEs

The S-1 subsystem of S-net is located off the Boso peninsula, where SSEs occur on a regular basis. The significant crustal deformation that was associated with an event in June 2018 was captured by terrestrial GNSS observations (Ozawa et al., 2019). An event at almost the same location also occurred in 2014, and Sato et al. (2017) reported that associated vertical seafloor movement of ~ 2 cm was detected by OBPR observations. According to Ozawa et al. (2019), the event in 2018, which was the first following deployment of the S-net, was larger in scale than that in 2014, and the seafloor displacement should have been captured by the S-net seafloor pressure observations. The records of the four S-net stations closest to the SSE source estimated by Ozawa et al (2019), with small LPRs (1–07: 0.67, 1–08: 1.47, 1–11: 1.03, 1–22: 1.23) following temperature correction and common component removal by PCA, are shown in Fig. 9. PCA was performed on the records of four stations. The RMS amplitude of the OBPR records was evaluated to be 1 hPa when Sato et al. (2017) observed the crustal deformation associated with the 2014 event. An RMS of 3.10 hPa (5.2 hPa before common-mode reduction) was observed in the post-processing record for 1–12, which is closest to the epicenter; however, the high noise level of the S-net pressure data rendered it difficult to detect the tectonic

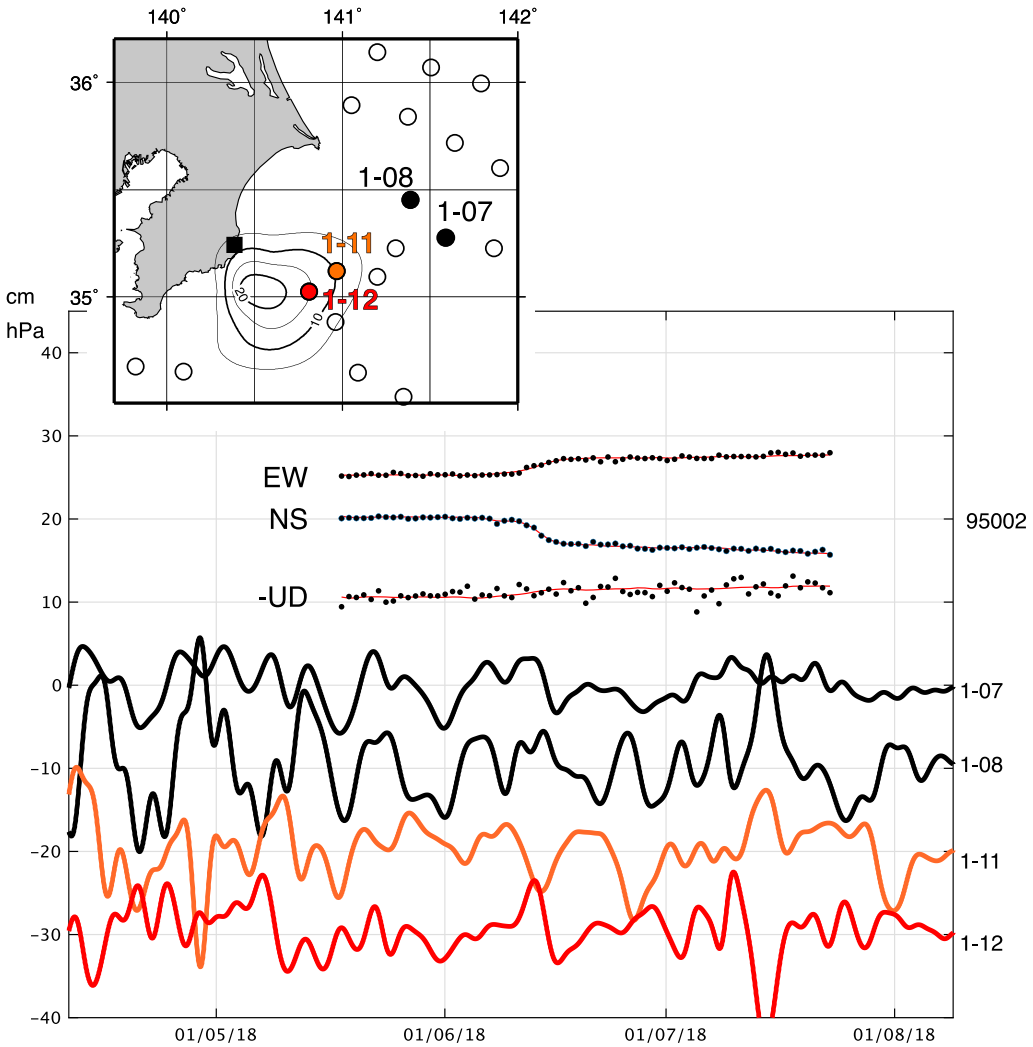

Fig. 9 S-net pressure records during 2018 Boso SSE. Records at four relatively quiet stations (indicated by colored circles in the inset) are shown. Records at other noisy S-net stations (shown in open circles) are not shown. Three components terrestrial GNSS data are also indicated. Note that vertical component is flipped in sign so that positive change means subsidence and is equivalent to a pressure increase on the seafloor. Slip distribution (Ozawa et al., 2019, contours in cm) is shown in the inset

signals corresponding to the 2018 SSE, although it was larger (Mw 6.8) in scale than the 2014 event (Mw 6.5).

It has been pointed out that the SSEs comprise the background of the increased activity that is associated with tectonic tremor in many subduction zones. Since tremors occur constantly in the northern Japan Trench region where subsystem S-4, which includes several quiet stations, is located, we investigated whether any significant fluctuations associated with tremor activity can be observed in the S-net seafloor pressure records. The target period of August 2016 to August 2018 was selected because tremor activity has been reported by Nishikawa et al. (2019) for some of this period. We focused on the data at station 4–22, which was closest to the tremor area and has the lowest LPR among the S-4 stations. As in the previous section, PCA analysis and calculation of the pressure difference from a reference point were used. Since an anomalous large fluctuation was observed in the data prior to October 2017 at 3–20, which is the reference point for differential pressure, only the differential pressure after this date was used. The resulting waveforms are shown in Fig. 10. The RMS of the records for 4–22 was 1.10 hPa following noise reduction with PCA using the S-4 data set, and the RMS amplitude for the differential pressure record was 1.41. We compared the temporal changes of the tectonic microtremor activity with the processed records but could not find any change in the tectonic microtremor activity that could be associated with increases in tremor activity. Although the noise level was much lower than that of S-1 off Boso, the scale of the SSE-associated tremor bursts occurring in this area is much smaller than that of the Boso SSEs, rendering it difficult to detect such transient tectonic events using S-net.

Hino et al. (2014) discussed the relationship between the OBPR noise levels and the detection ability of SSE.

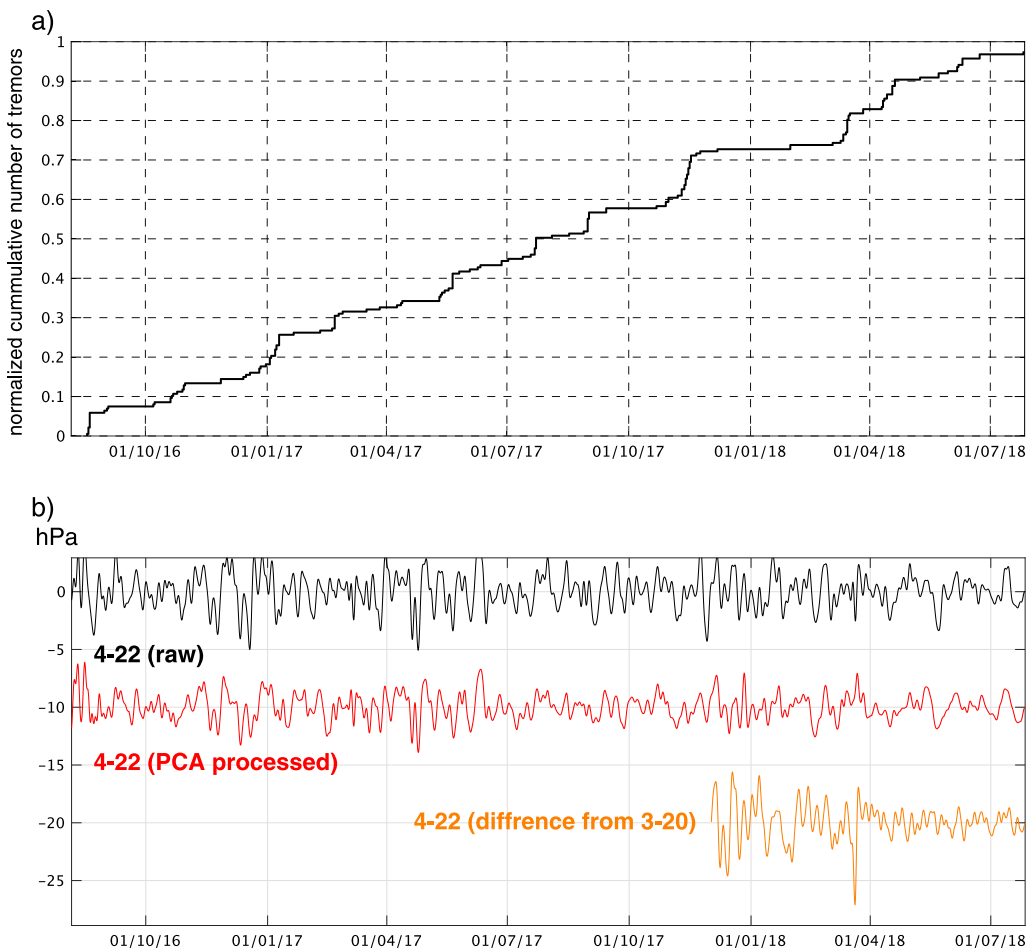

Fig. 10 Tectonic tremor activity and S-net pressure records from 2016 to 2018 in the northern Japan Trench. **a** Cumulative number of tremors. **b** Pressure record at station 4–22, the closest station to the tremor swarm. Black: Temperature-corrected trace. Red: Trace after common-mode reduction using PCA. Orange: Pressure difference from station 3–20

They reported RMS amplitudes of ~ 1.5 hPa for the analyzed OBPR records, which were reduced by ~ 0.5 hPa to ~ 1.0 hPa following PCA-based noise reduction. They further estimated the lower detection limit of the slip events by considering the noise level of the OBPR records and concluded that events of Mw 6.0 or larger that occur on shallow plate boundaries near the trench can be detected by nearby OBPRs. The RMS amplitude at station 4–22 was comparable to those of the OBPRs, and we therefore assume that the station has the same level of detection capability for tectonic transients. Therefore, possible SSEs that yield repeating tremor bursts in the northern Japan Trench would not be significantly larger than ~ Mw 6, the possible size of detectable SSEs taking place immediately below the quiet S-net stations.

Honsho et al. (2019) suggested that an SSE occurred along the shallow subduction interface in the northern Japan Trench in 2015, prior to the S-net deployment, based on small repeating earthquakes and seafloor horizontal motions observed using GNSS-A. The source location is located within the coverage of the S-4 subsystem and its magnitude is estimated to have been Mw 6.5. If an SSE of similar magnitude were to occur in the future, S-net would certainly be able to detect the crustal deformation. The vertical motions obtained by S-net, together with the horizontal displacements obtained by the GNSS-A, will thus play an important role in constraining the source model of SSEs.

As a case study, we examined the detectability of crustal deformation in a simple manner, focusing on two regions. For events that are likely to occur repeatedly, such as those in the northern Japan Trench, significant crustal deformation could be identified by stacking the noisy data referring to the timings of tremor burst events (e.g., Frank et al., 2015). However, owing to the high noise level, accumulating data to increase the number of stacking is important.

To improve the detection of tectonic signals related to SSEs, it is also necessary to improve the performance of reduction in common-mode variations originating from non-tidal oceanographic fluctuations. It is essential to understand the spatiotemporal characteristics of the common-mode components, and comprehensive studies performed by changing the combinations of the used for the analyses will be an important subject. Milliner et al. (2018) discussed the superiority of independent component analysis (ICA) over PCA when it is applied to the decomposition of components with non-Gaussian distribution. Fluctuations of seafloor pressure are likely to follow non-Gaussian distribution, and application of ICA to the pressure data obtained by the seafloor network is worth investigating in the future.

Based on our evaluation, a third of the S-net stations were as quiet as the OBPR observations and can be used for monitoring the SSE activity in the region. Considering the uneven distribution of the station and large variation in noise levels across stations, pragmatic assessment of detectability based on numerical modeling is another important scope for future study.

4.2 Characteristics of seafloor temperature data

As the noise level of S-net was greatly reduced by the temperature correction, we expected that the noise level of the pressure data is strongly related to the temperature variation. Here, we examine the power spectrum of the temperature data.

The most significant influence on the characteristics of temperature variation observed by S-net is the location at which the instruments were deployed on the seafloor. Instruments are covered by sediments and are thus not in direct contact with seawater at depths shallower than 1500 m; thus, the temperature environment is significantly different from that of instruments that are not buried. The significantly higher mean temperature of ~ 10 °C for buried stations is due to the effects of the insulating sediment cover. Self-heating of the observation equipment accounts for the significantly high temperature observed at the buried stations. In a buried environment, the generated heat is retained and not transferred to the seawater effectively.

The power spectra of the buried stations and the stations exposed to seawater are shown in Fig. 11a and b, respectively. The spectra for the buried stations show a steep slope, reflecting the suppression of short-period temperature changes because of the thermal insulation. The power of the temperature spectrum is very low in the frequency band in terms of the LPR, and the temperature-correlated noise is expected to be small in the buried stations. The LPR tends to be smaller at stations shallower than 1500 m in Fig. 3b.

The spectra of the unburied stations have smaller fall-off slopes and higher temperature fluctuation levels than those of the buried stations. Although the temperature variation tends to be greater at stations located at shallower depth, no significant depth dependence is observed in the LPR distribution (Fig. 3b). The power spectra of the temperature data obtained by the OBPRs are superimposed in Fig. 11. Unlike the pressure data spectrum, the OBPR spectral shape is not significantly different from that of the unburied S-net stations. This means that self-heating has little effect on the temperature data obtained at unburied stations.

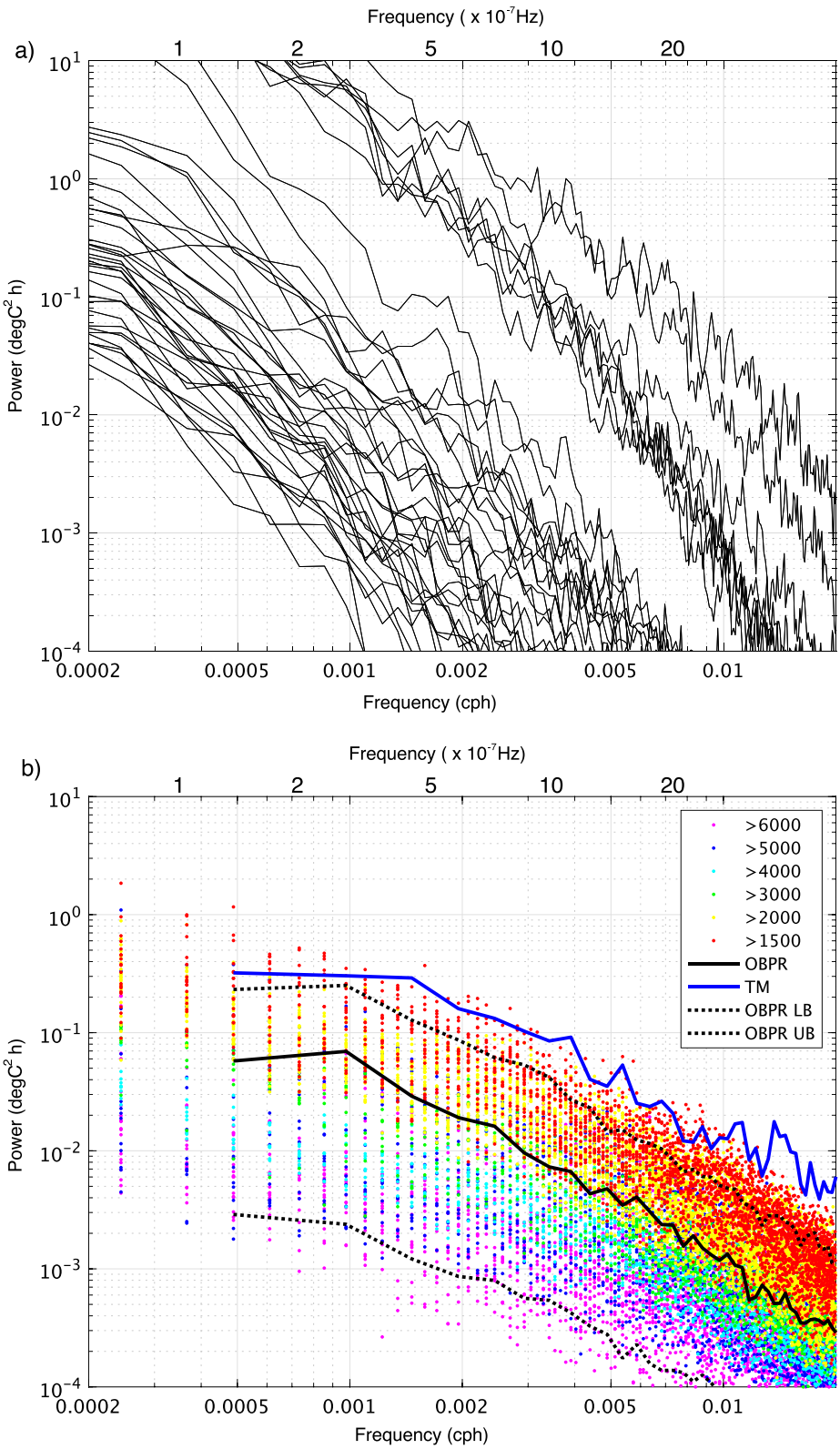

Fig. 11 Power spectra of temperature data at S-net stations. **a** Buried stations. **b** Unburied stations. Dot colors show the difference in station depths. Thick black line shows the median of the OBPR spectra and dotted lines are 25 and 75 percentiles. Blue denotes the average from TM stations

4.3 Possible mechanism of temperature-correlated noise

The temperature-correlated noise, a major reason for the large noise level in the S-net pressure observations, may be a result of the actual structure of the S-net observation system. The noise character is very similar to that of the pressure records obtained by the off-Sanriku cabled system (Inazu and Hino, 2011), hereafter the TM system. The TM system was also designed as an "inline system," and the structure of the observation unit was almost identical to that of S-net. The shape of the pressure power spectrum for the TM system was in the range of the spectra obtained for Group 2 in this study, indicating similarity to most S-net stations (Additional file 4: Fig. S4). The shape of the temperature spectrum was also similar to that of the unburied S-net stations (Fig. 11). The correlation between the pressure and temperature data obtained by the TM system and calculated in the same manner as the S-net data was very high (cross-correlation ~ 0.9) and a negative (−2 h) lag time was also observed. The strong dependence of the TM system on pressure data has already been pointed out by Inazu and Hino (2011). As indicated by Baba et al. (2006) and Itoh et al. (2019), the cabled system that was deployed off Hokkaido, another inline system, also showed a high correlation between pressure and temperature.

In contrast, there were no significant correlations between the pressure and temperature records obtained by the OBPR deployed in the Japan Trench, as pointed out earlier. Gomberg et al. (2019) investigated the relationship between seafloor pressure and temperature observed in the Hikrangi subduction zone, New Zealand, using the instruments of almost identical structure with the OBPRs deployed in Japan. Although they pointed out small correlations in time scale of ~ 10 d, the correlations were insignificant at lag times ~ 0 d. This report is consistent with our OBPR observations, but completely different from the characteristics identified in the S-net data, or in other inline observation systems.

Based on the similarity among the data obtained for inline systems, we suggest that the correlation between the pressure and temperature records is related to the mechanical structure of the inline system. The sensors comprising the inline system are not in direct contact with seawater, and bulkheads constructed using flexible materials, such as the bellows or the diaphragm, affect the results. If their motions were smooth, the internal pressure measured by the pressure sensor is expected to be in equilibrium with the seafloor pressure; otherwise, a pressure differential is created. However, the pressure transfer is insufficient and the internal and external pressures are not in equilibrium when the bulkheads are not in ideal conditions. Under poor pressure transfer conditions, the internal pressure is affected by the thermal deformation of the enclosure. This may be why the pressure data correlated with temperature change and qualitatively explains the time lag between temperature and pressure observed by S-net. Pressure responds instantaneously to temperature changes in the enclosure, but the measured lag in temperature change occurs because the sensors are thermally shielded.

At several S-net stations, sudden and extremely large (> 1000 hPa) pressure increases were observed with no corresponding change in temperature, indicating that the pressure step is neither due to temperature change nor a failure in the measurement or data transmission system. These incremental changes could correspond to events that have occurred spontaneously in the bulkheads, eliminating the disparity between internal and external pressure. The pressure transfer mechanism, including the bulkhead, is composed of several parts made of different materials. If we assume friction along the contact surfaces accounts for the pressure disparity, the events could be slips on the surfaces. Some of these pressure steps were accompanied by a marked decrease in the LPR. In the case shown in Additional file 5: Fig. S5, the power of the pressure signal following the change was reduced to the level of the OBPR spectrum. We interpret that the event corresponding to this change improved the pressure transfer performance, thus reducing the noise level. This observation supports the hypothesis that imperfect pressure transfer is a significant source of noise in the S-net data.

5 Conclusions

If small vertical crustal deformations can be detected using long-term, wide-area seafloor pressure observation data from S-net, significant progress in understanding the SSEs occurring at shallow plate boundaries along the Japan and the Kuril Trenches can be made. We therefore investigated the data obtained over the 7 years since S-net started operation in 2016 to ascertain whether the results obtained are suitable for geodetic application by evaluating the power spectra and correlations with temperature variation. Comparisons with data obtained by OBPR observations accumulated in the Japan Trench, which have previously been proven useful in geodetic studies, were used to characterize the quality of the S-net data for periods > 2 d, over which geodetic signals are expected to emerge.

The seafloor pressure data obtained at most S-net stations contained large fluctuations that are > 100-fold those obtained by OBPRs in terms of power. Owing to the extremely high noise level, detecting tectonic transients below the level of a few centimeters, which are associated with SSEs at these noisy stations, was difficult. The noise in the pressure data is strongly

correlated to temperature, which was simultaneously observed at the same station. Although no significant pressure–temperature correlations were identified in the OBPR data, a high correlation has been reported in previous studies and was confirmed in this study for the data obtained by seafloor-cabled observation systems other than S-net. We suggest that the temperature dependence accounts for the high noise level and may be caused by the mechanical structure characteristics of the inline systems. Furthermore, we devised a method to remove the temperature-correlated noise by applying a prediction filter to the S-net pressure records. Although the filter reduced the noise significantly, pressure records at more than half of the S-net stations still have large fluctuations that are more than 10 times more powerful than those observed in the OBPR data.

Based on processed records from stations with relatively low noise, we investigated whether any pressure changes corresponded to the 2018 Boso SSE or to possible SSEs associated with repetitive tectonic tremor bursts in the northern part of the Japan Trench. The noise level at the stations near the source of the Boso SSE meant that we could not detect any meaningful pressure change associated with the 2018 event (Mw 6.5). More than 10 stations have noise levels similar to, or slightly higher than, those associated with the OBPRs in the northern part of the Japan Trench. However, no transient changes were detected in the seafloor pressure corresponding to the reported tremor bursts from 2016 to 2018. Based on previous studies focusing on detection capability evaluated using OBPR records, we believe that the S-net can detect geodetic signals in the northern Japan Trench if SSEs larger than ~ Mw 6 occur in the vicinity of at least one station.

Abbreviations

S-net: Seafloor observation network for earthquakes and tsunamis along the Japan Trench; OBPR: Ocean bottom pressure recorder; SSE: Slow slip event; DONET: Dense Ocean floor Network system for Earthquakes and Tsunamis; RMS: Root mean squares; LPR: Logged power ratio; NIED: National research institute for earth science and disaster resilience.

Supplementary Information

The online version contains supplementary material available at https://doi.org/10.1186/s40645-022-00526-y.

Additional file 1: Fig. S1. a Example of power spectra obtained using data from a S-net station. Spectrum fluctuations over time at single stations indicated by the scattering of gray lines. Black line indicates the median and defines the representative shape of the power spectrum for the station. **b** Representative power spectra for all S-net stations. **c** Histograms showing power spectra of the 150 stations shown in b. Probability density defined by normalized frequency is shown according to the color code.

Additional file 2: Fig. S2. Probability density of pressure power spectra observed by OBPRs.

Additional file 3: Fig. S3. Pressure records after the temperature correction at stations with LPR < 1 (same as shown in Fig. 7a) with the first principal component (1st PC). The 1st PC is indicated at the top by a thick trace. **b** Pressure records after subtracting the 1st PC.

Additional file 4: Fig. S4. Probability density of pressure power spectra by S-net. Medians of OBPR and TM system superimposed onto the S-net histogram.

Additional file 5: Fig. S5. a Example of S-net pressure (black) and temperature (red) data. An extremely large step in pressure occurred in January 2020. **b** Power spectra of pressure data before (period I) and after the pressure step (period II).

Acknowledgements

We thank Prof. Roland Bürgmann and an anonymous reviewer and the Editor Takeshi Iinuma for their review of the manuscript and insightful comments. We also thank Syuichi Suzuki and Makiko Sato for their assistance in OBPR observations and data curation and Dr. Shozaburo Ozawa of Geospace Authority Japan for his kind provision of the geodetic data and the slip model describing the 2018 Boso SSE. Some figures were created using generic mapping tools (Wessel and Smith 1991). We would like to thank Editage (www.editage.com) for English language editing.

Author contributions

RH, TK, and NC proposed the topic and conceived and designed the study. RH, TK, YO, and HO carried out the experimental study. RH analyzed the data and helped with data interpretation. All the authors collaborated with the corresponding author in the drafting of the manuscript. All authors have read and approved the final manuscript.

Funding

This work was partly supported by JSPS KAKENHI Grant Number 19H05596.

Availability of data and materials

The S-net pressure gauge data are available at the Web site of the National Research Institute for Earth Science and Disaster Resilience (NIED 2019; https://doi.org/10.17598/NIED.0007). The OBPR data obtained by Tohoku University are available from the corresponding author upon request.

Declarations

Competing interests

The authors declare that they have no competing interests.

Author details

[1]Graduate School of Science, Tohoku University, 6-6 Aramaki-Aza-Aoba, Aoba-Ku, Sendai, Miyagi 980-8578, Japan. [2]National Research Institute for Earth Science and Disaster Resilience, 3-1 Tennodai, Tsukuba, Ibaraki 305-0006, Japan.

Received: 8 September 2022 Accepted: 24 November 2022
Published online: 30 December 2022

References

Aoi S, Asano Y, Kunugi T, Kimura T, Uehira K, Takahashi N, Ueda H, Shiomi K, Matsumoto T, Fujiwara H (2020) MOWLAS: NIED observation network for earthquake, tsunami and volcano. Earth Planets Space 72:126. https://doi.org/10.1186/s40623-020-01250-x

Baba T, Hirata K, Hori T, Sakaguchi H (2006) Offshore geodetic data conducive to the estimation of the afterslip distribution following the 2003 Tokachi-oki earthquake. Earth Planet Sci Lett 241:281–292. https://doi.org/10.1016/j.epsl.2005.10.019

Baba S, Takeo A, Obara K, Matsuzawa T, Maeda T (2020) Comprehensive detection of very low frequency earthquakes off the Hokkaido and Tohoku Pacific coasts Northeastern Japan. J Geophys Res. https://doi.org/10.1029/2019JB017988

Bürgmann R, Chadwell D (2014) Seafloor geodesy. Annu Rev Earth Planet Sci 42:509–534. https://doi.org/10.1146/annurev-earth-060313-054953

Davis EE, Villinger H, Sun T (2015) Slow and delayed deformation and uplift of the outermost subduction prism following ETS and seismogenic slip events beneath Nicoya Peninsula, Costa Rica. Earth Planet Sci Lett 410:117–127. https://doi.org/10.1016/j.epsl.2014.11.015

Dobashi Y, Inazu D (2021) Improving detectability of seafloor deformation from bottom pressure observations using numerical ocean models. Front Earth Sci 8:598270. https://doi.org/10.3389/feart.2020.598270

Frank WB, Radiguet M, Rousset B, Shapiro NM, Husker LM, Kostoglodov V, Cotte N, Campillo M (2015) Uncovering the geodetic signature of silent slip through repeating earthquakes. Geophys Res Lett 42:2774–2779. https://doi.org/10.1002/2015GL063685

Fredrickson EK, Wilcock WSD, Schmidt DA, MacCready P, Roland E, Kurapov AL, Zumberge MA, Sasagawa GS (2019) Optimizing sensor configurations for the detection of slow-slip earthquakes in seafloor pressure records, using the Cascadia Subduction Zone as a case study. J Geophys Res Solid Earth 124:13504–13531. https://doi.org/10.1029/2019JB018053

Fujiwara T, Kodaira S, No T, Kaiho Y, Takahashi N, Kaneda Y (2011) The 2011 Tohoku-Oki earthquake: Displacement reaching the trench axis. Science 334:1240. https://doi.org/10.1126/science.1211554

Gomberg J, Hautala S, Johnson P, Chiswell S (2019) Separating sea and slow slip signals on the seafloor. J Geophys Res 124:13486–13503. https://doi.org/10.1029/2019JB018285

Heki K, Miyazaki S, Tsuji H (1997) Silent fault slip following an interplate thrust earthquake at the Japan trench. Nature 386:595–598. https://doi.org/10.1038/386595a0

Hino R, Inazu D, Ohta Y, Ito Y, Suzuki S, Iinuma T, Osada Y, Kido M, Fujimoto H, Kaneda Y (2014) Was the 2011 Tohoku-Oki earthquake preceded by aseismic preslip? Examination of seafloor vertical deformation data near the epicenter. Mar Geophys Res 35:181–190. https://doi.org/10.1007/s11001-013-9208-2

Hirata K, Aoyagi M, Mikada H, Kawaguchi K, Kaiho Y, Iwase R, Morita S, Fujisawa I, Sugioka H, Mitsuzawa K, Suyehiro K, Kinoshita H, Fujiwara N (2002) Real-time geophysical measurements on the deep seafloor using submarine cable in the Southern Kurile subduction zone. IEEE J Oceanic Eng 27:170–181. https://doi.org/10.1109/JOE.2002.1002471

Honsho C, Kido M, Tomita F, Uchida N (2019) Offshore postseismic deformation of the 2011 Tohoku earthquake revisited: Application of an improved GPS-acoustic positioning method considering horizontal gradient of sound speed structure. J Geophys Res 124:5990–6009. https://doi.org/10.1029/2018JB017135

Iinuma T, Hino R, Kido M, Inazu D, Osada Y, Ito Y, Ohzono M, Tsushima H, Suzuki S, Fujimoto H, Miura S (2012) Coseismic slip distribution of the 2011 off the Pacific coast of Tohoku Earthquake (M9.0) refined by means of seafloor geodetic data. J Geophys Res 117:B07409. https://doi.org/10.1029/2012JB009186

Iinuma T, Hino R, Uchida N, Nakamura W, Kido M, Osada Y, Miura S (2016) Seafloor observations indicate spatial separation of coseismic and postseismic slips in the 2011 Tohoku earthquake. Nat Commun 7:13506. https://doi.org/10.1038/ncomms13506

Inazu D, Hino R (2011) Temperature correlation and usefulness of ocean bottom pressure data from cabled seafloor observation around Japan and for analyses of tsunami, ocean tides, and low-frequency geophysical phonemena. Earth Planets Space 63:1133–1149. https://doi.org/10.5047/eps.2011.07.014

Inazu D, Hino R, Fujimoto H (2012) A global barotropic ocean model driven by synoptic atmospheric disturbances for detecting seafloor vertical displacements from in situ ocean bottom pressure measurements. Mar Geophys Res 33:127–148. https://doi.org/10.1007/s11001-012-9151-7

Inoue T, Ito Y, Wallace LM, Yoshikawa Y, Inazu D, Garcia ESM, Muramoto T, Webb SC, Ohta K, Suzuki S, Hino R (2021) Water depth dependence of long-range correlation in nontidal variations in seafloor pressure. Geophys Res Lett. https://doi.org/10.1029/2020GL092173

Ito Y, Hino R, Kido M, Fujimoto H, Osada Y, Inazu D, Ohta Y, Iinuma T, Ohzono M, Miura S, Mishina M, Suzuki K, Tsuji T, Ashi J (2013) Episodic slow slip events in the Japan subduction zone before the 2011 Tohoku-Oki earthquake. Tectonophys 600:14–26. https://doi.org/10.1016/j.tecto.2012.08.022

Ito Y, Hino R, Suzuki S, Kaneda Y (2015) Episodic tremor and slip near the Japan Trench prior to the 2011 Tohoku-Oki earthquake. Geophys Res Lett 42:1725–1731. https://doi.org/10.1002/2014GL062986

Itoh Y, Nishimura T, Ariyoshi K, Matsumoto H (2019) Interplate slip following the 2003 Tokachi-oki earthquake from ocean bottom pressure gauge and land GNSS data. J Geophys Res Solid Earth 124:4205–4230. https://doi.org/10.1029/2018JB016328

Kanazawa T, Hasegawa A (1997) Ocean-bottom observatory for earthquakes and tsunami off Sanriku, north-eastern Japan using submarine cable. In: proceedings of international workshop on scientific use of submarine cables.

Katakami S, Ito Y, Ohta K, Hino R, Suzuki S, Shinohara M (2018) Spatiotemporal variation of tectonic tremor activity before the Tohoku-Oki earthquake. J Geophys Res 123:9676–9688. https://doi.org/10.1029/2018JB016651

Kato A, Obara K, Igarashi T, Tsuruoka H, Nakagawa S, Hirata N (2012) Propagation of slow slip leading up to the 2011 Mw 90 Tohoku-Oki earthquake science. Bull Seismol Soc Am 335:705–708. https://doi.org/10.1126/science.1215141

Kawasaki I, Asai Y, Tamura Y, Sagiya T, Mikami N, Okada Y, Sakata M, Kasahara M (1995) The 1992 Sanriku-Oki, Japan, ultra-slow earthquake. J Phys Earth 43:105–116. https://doi.org/10.4294/jpe1952.43.105

Kodaira S, Fujiwara T, Fujie G, Nakamura Y, Kanamatsu T (2020) Large coseismic slip to the trench during the 2011 Tohoku-oki earthquake. Annu Rev Earth Planet Sci 48:321–343. https://doi.org/10.1146/annurev-earth-071719-055216

Kubota T, Saito T, Suzuki W (2020) Millimeter-scale tsunami detected by a wide and dense observation array in the deep ocean: fault modeling of an Mw 60 interplate earthquake off Sanriku NE Japan. Geophys Res Lett. https://doi.org/10.1029/2019GL085842

Kubota T, Saito T, Chikasada NY, Sandanbata O (2021a) Meteotsunami observed by the deep-ocean seafloor pressure gauge network off northeastern Japan. Geophys Res Lett. https://doi.org/10.1029/2021aGL094255

Kubota T, Kubo H, Yoshida K, Chikasada NY, Suzuki W, Nakamura T, Tsushima H (2021b) Improving the constraint on the Mw 7.1 2016 Off-Fukushima shallow normal-faulting earthquake with the high azimuthal coverage tsunami data from the S-net wide and dense network: implication for the stress regime in the Tohoku overriding plate. J Geophys Res Solid Earth. https://doi.org/10.1029/2021JB022223

Kubota T, Saito T, Nishida K (2022) Global fast-traveling tsunamis driven by atmospheric lamb waves on the 2022 Tonga eruption. Science 377:91–94. https://doi.org/10.1126/science.abo4364

Matsuzawa T, Asano Y, Obara K (2015) Very low frequency earthquakes off the Pacific coast of Tohoku, Japan. Geophys Res Lett 42:4318–4325. https://doi.org/10.1002/2015GL063959

Milliner C, Materna K, Bürgmann R, Fu Y, Moore AW, Bekaert D, Adhikari S, Argus DF (2018) Tracking the weight of Hurricane Harvey's stormwater using GPS data. Sci Adv. https://doi.org/10.1126/sciadv.aau2477

Muramoto T, Ito Y, Inazu D, Wallace LM, Hino R, Suzuki S, Webb SC, Henrys S (2019) Seafloor crustal deformation on ocean bottom pressure records with non-tidal variability corrections: application to Hikurangi margin, New Zealand. Geophys Res Lett 46:303–310. https://doi.org/10.1029/2018GL080830

National research institute for earth science and disaster resilience [NIED] (2019) NIED S-net. https://doi.org/10.17598/nied.0007

Nishikawa T, Matsuzawa T, Ohta K, Uchida N, Nishimura T, Ide S (2019) The slow earthquake spectrum in the Japan Trench illuminated by the S–net seafloor observatories. Science 365:808–813. https://doi.org/10.1126/science.aax5618

Obara K, Kato A (2016) Connecting slow earthquakes to huge earthquakes. Science 353:253–257. https://doi.org/10.1126/science.aaf1512

Ohta Y, Hino R, Inazu D, Ohzono M, Ito Y, Mishina M, Iinuma T, Nakajima J, Osada Y, Suzuki K, Fujimoto H, Tachibana K, Demachi T, Miura S (2012) Geodetic constraints on afterslip characteristics following the March 9, 2011, Sanriku-oki earthquake. Japan Geophys Res Lett 39:L16304. https://doi.org/10.1029/2012GL052430

Ohta K, Ito Y, Hino R, Ohyanagi S, Matsuzawa T, Shiobara H, Shinohara H (2019) Tremor and inferred slow slip associated with afterslip of the 2011 Tohoku Earthquake. Geophys Res Lett 46:4591–4598. https://doi.org/10.1029/2019GL082468

Ozawa S, Yarai H, Kobayashi T (2019) Recovery of the recurrence interval of Boso slow slip events in Japan. Earth Planets Space 71:78. https://doi.org/10.1186/s40623-019-1058-y

Polster A, Fabian M, Villinger H (2009) Effective resolution and drift of Paroscientific pressure sensors derived from long-term seafloor measurements. Geochem Geophys Geosyst 10:Q08008. https://doi.org/10.1029/2009GC002532

Sato T, Hasegawa S, Kono A, Shiobara H, Yagi T, Yamada T, Shinohara M, Usui N (2017) Detection of vertical motion during a slow-slip event off the Boso Peninsula Japan, by Ocean bottom pressure gauges. Geophys Res Lett 44:2710–2715. https://doi.org/10.1002/2017GL072838

Suzuki K, Nakano M, Takahashi N, Hori T, Kamiya S, Araki E, Nakata R, Kaneda Y (2016) Synchronous changes in the seismicity rate and ocean-bottom hydrostatic pressures along the Nankai trough: a possible slow slip event detected by the dense oceanfloor network system for Earthquakes and Tsunamis (DONET). Tectonophysiscs 680:90–98. https://doi.org/10.1016/j.tecto.2016.05.012

Tanaka S, Matsuzawa T, Asano Y (2019) Shallow low-frequency tremor in the Northern Japan Trench subduction zone. Geophys Res Lett 46:5217–5224. https://doi.org/10.1029/2019GL082817

Uchida N, Iinuma T, Nadeau RM, Bürgmann R, Hino R (2016) Periodic slow slip triggers megathrust zone earthquakes in northeastern Japan. Science 351:488–492. https://doi.org/10.1126/science.aad3108

Wallace LM, Webb SC, Ito Y, Mochizuki K, Hino R, Henrys S, Schwartz SY, Sheehan AF (2016) Slow slip near the trench at the Hikurangi subduction zone, New Zealand. Science 352:701–704. https://doi.org/10.1126/science.aaf2349

Watts DR, Kontoyiannis H (1990) Deep-ocean bottom pressure measurements: drift removal and performance. J Atmos Ocean Technol 7:296–306. https://doi.org/10.1175/1520-0426(1990)007

Watts DR, Wei M, Tracey KL, Donohue KA, He B (2021) Seafloor geodetic pressure measurements to detect shallow slow slip events: methods to remove contributions from ocean water. J Geophys Res Solid Earth. https://doi.org/10.1029/2020JB020065

Wessel P, Smith WHF (1991) Free software helps map and display data. Eos Trans Am Geophys Union 72:441–446. https://doi.org/10.1029/90EO00319

Wilcock WSD, Manalang DA, Fredrickson EK, Harrington MJ, Cram G, Tilley J, Burnett J, Martin D, Kobayashi T, Paros JM (2021) A thirty-month seafloor test of the A-0-A method for calibrating pressure gauges. Front Earth Sci 8:600671. https://doi.org/10.3389/feart.2020.600671

Publisher's Note